

Topology optimization of low-friction painting distribution on a marine propeller

Eduardo Tadashi Katsuno^{1*}, João Lucas Dozzi Dantas² and Emílio Carlos Nelli Silva¹

^{1*}Department of Mechatronics and Mechanical Systems Engineering, University of São Paulo, Escola Politécnica, 2231 Prof. Mello Moraes Ave., São Paulo, 05508-030, São Paulo, Brazil.

²Energy Infrastructure Laboratory, Institute for Technological Research, 532 Prof. Almeida Prado Ave., São Paulo, 05508-901, São Paulo, Brazil.

*Corresponding author(s). E-mail(s): eduardo.katsuno@uni-due.de,
<https://orcid.org/0000-0003-2818-3518>;

Contributing authors: joao.dantas@strath.ac.uk, <https://orcid.org/0000-0002-6482-0222>;
ecnsilva@usp.br, <https://orcid.org/0000-0003-1715-1713>;

Abstract

Following the United Nations 2030 Agenda to achieve a better and more sustainable future, there is an interest in new energy efficiency technologies to address emissions from international maritime shipping. A large portion of the available research focused on paints that reduce the fouling and friction of the hulls of these vessels, such as hydrophobic paints. Yet, research applied to propellers is smaller when compared to hulls. Covering the blade surface with hydrophobic paint behavior changes the drag of the propeller and, consequently, the hydrodynamic efficiency. However, covering a blade may adversely affect the flow in certain regions, reducing the propeller performance. This paper studies a practical application of the super-hydrophobic surface (SHS) pattern distribution on a marine propeller using the topology optimization method to determine regions where the application of surface treatment leads to improved propeller efficiency. The numerical method is developed to model the turbulent flow condition with the behavior of the boundary layer that imposes the low-friction/hydrophobicity effect to predict the performance of a coated propeller. To evaluate the proposed method, firstly, a fully covered blade is simulated for several hydrophobic conditions and then the topology optimization is conducted. Despite the SHS behavior being simplified by adopting the slip length model, the obtained optimization results show the regions to be prioritized in order to maximize the hydrodynamic efficiency.

Keywords: Propeller, CFD, Turbulent flow, Topology Optimization, SHS

1 Introduction

In 2015, the United Nations (UN) set up a 2030 Agenda - Sustainable Development Goals, describing 17 main goals to achieve a better and more sustainable future ([United Nations, 2015](#)). To address

the goal 13: *Climate Actions*, 196 parties signed the Paris Climate Agreement during COP 21 to limit global temperature rise to well below 2 °C. The International Maritime Organization (IMO), a specialized agency of the United Nations, published the relation of these goals into the maritime field, adopting the goal to reduce the total annual greenhouse gas emissions from international shipping by at least 50% by 2050 compared to 2008 (International Maritime Organization, 2015, 2018, 2021).

Considering the goals 7: *Affordable and Clean Energy* and 13: *Climate Actions*, International Maritime Organization (2015) suggests new energy efficiency technologies to address these emissions from international shipping and the adoption of the Energy Efficiency Design Index (EEDI) for the design of ships, being discussed in Longva et al (2010) on how to determine the EEDI based on a cost-effective criterion. For several years, shipyards and research centers in the Naval Architecture and Ocean Engineering area have studied the process of hull and propeller optimization to improve hydrodynamic efficiency of large vessels, obtaining high-end optimized hulls and propellers for each application. In order to increase the ship energy efficiency, research has been carried out on new technological solutions, such as the use of bubbles to reduce hull friction (Mäkiharju and Ceccio, 2018) or the assessment of energy efficiency of integrated electric propulsion (Nuchturee et al, 2020).

One of the main drawbacks of these technologies is that they depend on a new design of the vessel, being very difficult to be applied to an existing ship. At this point, another emerging research field in which it is intended to reduce hydrodynamic resistance and improve performance is about painting hulls and propellers with low-friction paints, such as paints that create hydrophobic surfaces. The application of these paints makes the hull a super-hydrophobic surface (SHS). Thus, vessels could increase their efficiency by just performing the proper paint maintenance (Fu et al, 2017).

In a recent report of The International Towing Tank Conference (2021), it is indicated an interest from industry and academia in high-efficiency vessels, by adopting frictional drag reduction methods. Riblets and textured surfaces, compliant surfaces, large-eddy breakup devices, SHS,

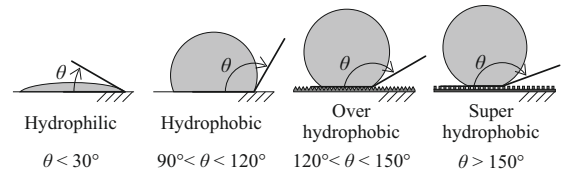


Fig. 1 Classification of SHS through water drop contact angle. Adapted from Muzenski et al (2015).

and coatings/paints are cited as passive methods to frictional drag reduction methods. Mutton et al (2005) presented a full-scale study, through a three-year follow-up of a vessel with and without anti-foil painting on the propeller. However, due to environmental implications, it was not possible to verify the performance difference, yet, the authors verified that the painted propeller presented a lower surface roughness than the propeller without the paint. Korkut and Atlar (2012) and Mutton et al (2005) conducted an experimental study on a model-scale propeller in a cavitation tunnel comparing the observed cavitation patterns in propellers with and without commercial paint. A small improvement of the cavitation was verified in uniform and non-uniform (wake condition) flows.

A super-hydrophobic surface can be defined by the angle of a droplet free-surface resting on it (Ou et al, 2004), as shown schematically in Fig. 1. These surfaces are commonly known to exhibit high repellency, being used in self-cleaning surfaces in several fields of engineering, from clothing (Cho et al, 2009), glasses (Park et al, 2011), and cementitious composites for highway applications (Muzenski et al, 2015).

In recent years, super-hydrophobic surface studies have intensified. Ou et al (2004) investigated the effect of drag reduction in laminar flow, comparing the numerical model with experimental results. Voronov et al (2006, 2007, 2008) studied the correlation of the contact angle with the slip length, a variable that defines the hydrophobicity. Super-hydrophobic studies were being led successfully for laminar flow, stimulating researchers to start the phenomena exploration in the turbulent flow context. Seo and Mani (2016) describes that the main difference between the flow behavior on SHS in laminar and turbulent regimes is the separation of scale between the length scale of the mean velocity gradients and that of macroscopic geometry. Min and Kim (2004) is one of the first

works to assess the effects of SHS using direct numerical simulation (DNS) with turbulence phenomena, observing that the SHS effect reduces the drag in the same direction of the flow and increases it in the case of perpendicular flow. In the maritime field, [Daniello et al \(2009\)](#) investigated the effect of a vessel in turbulent flows with an experimental approach, observing a significant drag reduction by particle image velocimetry (PIV) and direct pressure measurements. [Peifer et al \(2020\)](#) conducted some preliminary experiments to assess the feasibility of combining an SHS and air layer drag reduction. [Zhao et al \(2021\)](#) also conducted experiments using fluorescence correlation spectroscopy to observe the velocity profiles of SHS.

However, the research in SHS applied to propellers is smaller compared to hulls. The main effect of the hydrophobic painting is the reduction of the friction drag, varying thrust and torque. In a marine propulsion system, this variation needs to be designed to increase efficiency and reduce the overall cost. Hydrophobic surfaces are usually not cheap and should be applied according to established criteria. Other side effects may arise with the application, which should be further investigated.

To design the surface distribution of a super-hydrophobic paint, the Topology Optimization Method (TOM) is adopted. Unlike most topology optimization applications in fluid problems ([Borrvall and Petersson, 2003](#); [Evgrafov, 2005](#); [Gersborg-Hansen et al, 2005](#); [Othmer, 2008](#)), since the geometry is fixed, it is more feasible to use turbulence models easily.

Topology Optimization consists of changing design variables to improve a cost function value. In this work, design variables change the presence or absence of material (i.e., the presence or absence of super-hydrophobic paint) on the blade surface. The design procedure is illustrated in [Fig. 2](#).

Firstly, an initial domain is defined. Then, the domain is discretized and divided into elements, defining nodes and degrees of freedom. With the discretized domain, topology optimization takes place. The flow is solved and the cost function is computed, along with its sensitivities, being fundamental for gradient-based optimizers to determine the next iteration. The process continues until it reaches pre-defined stop criteria

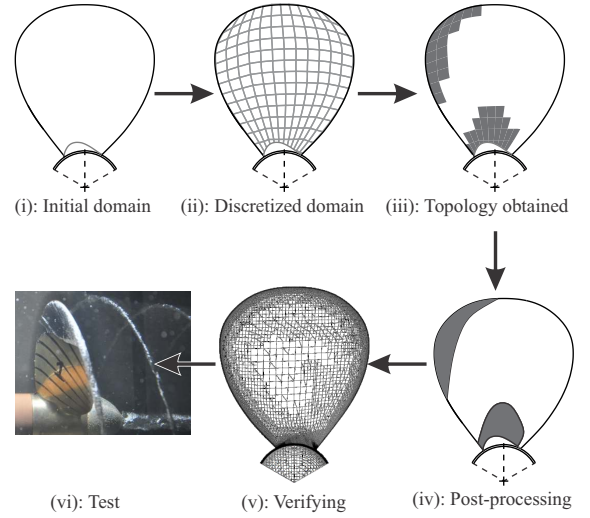


Fig. 2 Optimization procedure for surface topology optimization on a propeller blade.

that define the convergence of the material distribution. After the convergence, post-processing is performed and reevaluated numerically in a CFD analysis mesh, verifying the results. This verification step is essential to evaluate if the desired objective is reached even with the post-processed modifications. Finally, the experimental test can be performed. This stage requires the ability to reproduce the same hydrophobic conditions, with pre-established models, which is not the scope of this work.

This work has the objective of optimizing the pattern distribution of paint with super-hydrophobic properties on the surface of a model-scale marine propeller, with existing defined geometry, using the Topology Optimization Method, in order to increase the hydrodynamic efficiency. To accomplish this objective, firstly a method for propeller CFD simulations with SHS is developed, evaluating the super-hydrophobic levels on the hydrodynamic performance of the marine propeller. Then, TOM is used to design the distribution of the super-hydrophobic painting, observing in which blade regions it is important to prioritize the SHS in order to maximize the hydrodynamic efficiency.

2 Test case

The study is carried out with a Gawn-Burriel (KCA) systematic series propeller ([Gawn and](#)

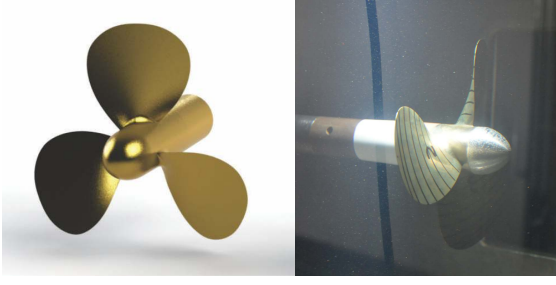


Fig. 3 CAD representation of propeller P104 (left); and inside of cavitation tunnel (right).

Burrill, 1957) called P104. The propeller is a 1:7 model-scale propeller that operates on a 200-ton boat. Pictures of P104 are shown in Fig. 3 and propeller design, in Fig. 4. It has three blades, diameter of 0.2 m, pitch-to-diameter ratio of 0.86, expanded area ratio of 0.50, and axis diameter of 0.038 m. Note that the propeller has a rounded tip, smoothing out the propeller edges.

The typical propeller performance indicators are the advance ratio J , thrust coefficient K_T , torque coefficient K_Q , and hydrodynamic efficiency η_0 . The advance ratio J can be interpreted as the propeller operating condition, relating the advance velocity, associated with the vessel velocity, and the propeller rotating rate. Thrust produced by the propeller and the required torque are usually presented in non-dimensional form, K_T and K_Q .

The η_0 is an important factor for the overall ship design as it can be interpreted as the ratio of the power needed to overcome the ship resistance by the rotational power needed by the engine to overcome the propeller torque. In other words, with an increase in efficiency, it is possible to navigate the ship with higher velocity or with lower consumption. Due to this importance, the η_0 is adopted as the cost function to be optimized. These properties are expressed as:

$$J = \frac{v_a}{nD_{\text{prop}}}, \quad K_T = \frac{T}{\rho n^2 D_{\text{prop}}^4}, \quad (1)$$

$$K_Q = \frac{Q}{\rho n^2 D_{\text{prop}}^5}, \quad \eta_0 = \frac{T v_a}{2\pi n Q} = \frac{J K_T}{2\pi K_Q}.$$

To analyze the resulted pressure and friction distributions on the blade, it is used the non-dimensional coefficients C_p and C_f , defined as:

$$C_p = \frac{2p}{\rho v_{\text{ref}}^2}, \quad C_f = \frac{2\|\boldsymbol{\tau}\|}{\rho v_{\text{ref}}^2}, \quad (2)$$

$$v_{\text{ref}} = \sqrt{v_a^2 + (0.7\pi n D_{\text{prop}})^2}.$$

In those equations, v_a is the advance velocity; n , rotation rate; D_{prop} , propeller diameter; ρ , fluid density; p , relative pressure; $\boldsymbol{\tau}$, shear stress; T , thrust force; and Q , torque. In this work these coefficients are used to better understand the effects of the SHS coating in the blade.

3 Methods for CFD simulations of propeller with SHS

The numerical simulations are conducted using the CFD software Siemens STAR-CCM+ 13 double-precision. As detailed in Siemens (2018), the software is based on the cell-centered finite volume method using an unstructured grid solver. STAR-CCM+ is also used for the mesh generator and post-processing.

3.1 Governing equations

The propeller simulations are assumed to be incompressible fully-turbulent flow, being based on steady-state Reynolds-averaged Navier–Stokes (RANS). A moving reference frame (MRF) approach (also called quasi-steady method) is used to consider the propeller rotation in steady-state simulation. The continuity f_c and momentum transport equations \mathbf{f}_m (Versteeg and Malalasekera, 2007) are given respectively by:

$$f_c : \oint \mathbf{u}_r \cdot d\mathbf{s} = 0, \quad (3)$$

$$\mathbf{f}_m : \oint \rho \mathbf{u} \otimes \mathbf{u}_r \cdot d\mathbf{s} + \int \rho \boldsymbol{\omega} \times \mathbf{u} d\Omega$$

$$+ \oint p \mathbf{I} \cdot d\mathbf{s} - \oint 2(\mu + \mu_t) \mathbf{D} \cdot d\mathbf{s} = 0, \quad (4)$$

in which \mathbf{u}_r is the relative velocity (defined as $\mathbf{u}_r = \mathbf{u} - \boldsymbol{\omega} \times \mathbf{r}$); \mathbf{u} , average vector of velocity; $\boldsymbol{\omega}$, angular velocity vector; \mathbf{r} , distance vector between origin and material point; \mathbf{s} , vector area; Ω , volume control; p , average value of pressure (included the contribution from turbulence kinetic

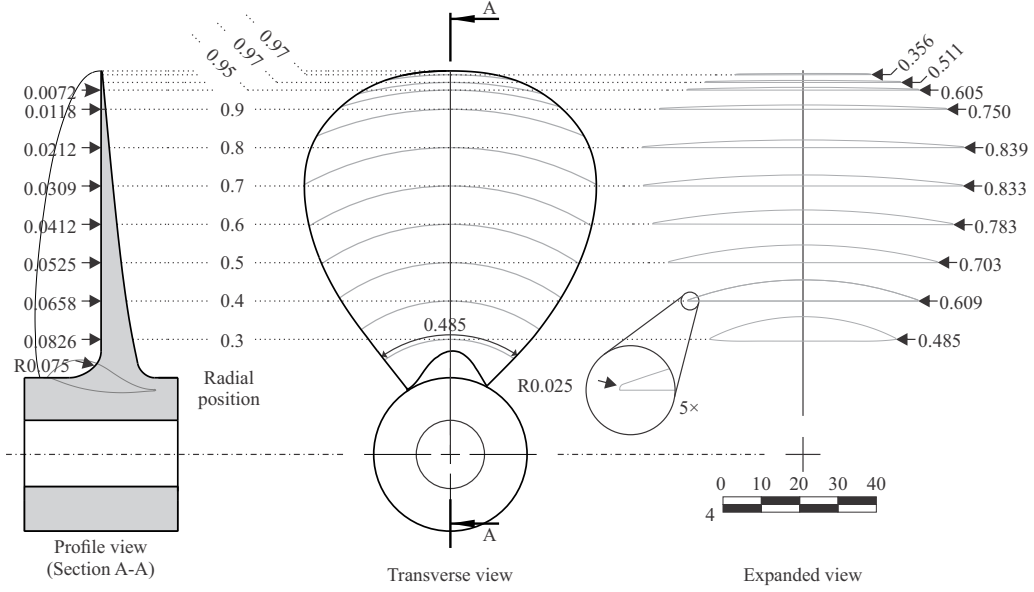


Fig. 4 Profile, transverse, and expanded view of P104 propeller. Units in meter.

energy, $2/3\rho k$); \mathbf{I} , identity tensor; k , turbulence kinetic energy; μ , molecular viscosity; μ_t , turbulent eddy viscosity; and \mathbf{D} , strain rate tensor, given by Eq. (5).

$$\mathbf{D} = \frac{1}{2} [\nabla \mathbf{u} + (\nabla \mathbf{u})^T]. \quad (5)$$

The $k - \omega$ SST turbulence model (Menter, 1994) is adopted in this work. Tests suggest that this turbulence model gives superior performance for zero pressure gradient and adverse pressure gradient boundary layers (Versteeg and Malalasekera, 2007).

This turbulence model adds two extra transport equations: for turbulence kinetic energy k and specific dissipation rate ω :

$$\begin{aligned} \nabla \cdot (\rho k \mathbf{u}) &= \nabla \cdot [(\mu + \sigma_k \mu_t) \nabla k] - \rho \beta^* f_{\beta^*} \omega k + P_k, \\ \nabla \cdot (\rho \omega \mathbf{u}) &= \nabla \cdot [(\mu + \sigma_\omega \mu_t) \nabla \omega] - \rho \beta f_\beta \omega^2 + P_\omega, \end{aligned} \quad (6)$$

in which P_k and P_ω are production terms; f_{β^*} , free-shear modification factor; f_β , vortex-stretching modification factor; σ_k and σ_ω , model coefficients. The turbulent eddy viscosity is given by:

$$\mu_t = \frac{a_1 \rho k}{\max(a_1 \omega, \|\mathbf{D}\| F_2)} \quad (7)$$

in which a_1 is a constant; $\|\mathbf{D}\|$, strain rate magnitude; and F_2 , blending function. The details of each term and its implementation are shown in Versteeg and Malalasekera (2007) and Siemens (2018).

3.2 Domain dimensions and boundary conditions

Considering the three blades of the propeller, the domain is a one-third cylinder. This simplification is acceptable once it uses RANS equations, which only model large eddies, and the main interest is at the mean values of thrust and torque. This simplification was used in other similar works, such as Wang et al (2010). The dimensions and boundary conditions are shown in Fig. 5. In this work, it is adopted the values of $d_x = 5$ and $d_z = 5$, the same values that were observed and compared with experiments in previous works (Katsuno and Dantas, 2017).

The numerical treatment for velocity inlet boundary conditions is that the velocity is specified, the pressure gradient is zero, and turbulence kinetic energy and specific dissipation rate are also specified. For pressure outlet boundary condition, velocity gradient is zero, the relative pressure is imposed to be zero, turbulence kinetic energy and specific dissipation rate gradients are zero. The

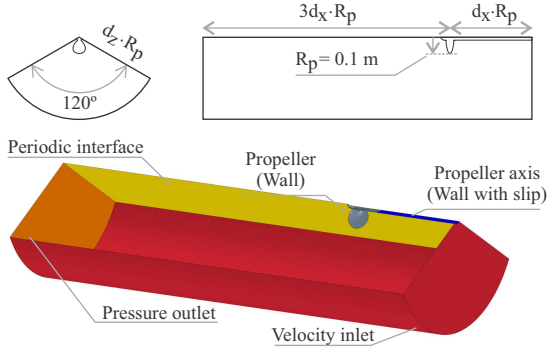


Fig. 5 Domain geometry and boundary conditions, adopting $d_x = 5$ and $d_z = 5$.

propeller is modeled as a wall boundary condition with SHS, further described in Sec. 3.3. For wall with slip, the normal component of velocity is defined as zero. In both cases, pressure and turbulence kinetic energy gradients are zero, and the specific dissipation rate is defined.

The moving reference frame (MRF) is used inside the domain to simulate the rotating effect, and a fixed reference frame is used to define the velocity inlet. Sánchez-Caja et al (2009) compared time-accurate propeller simulations with MRF and mixing-plane approach and concluded that MRF approach presented better prediction than the mixing-plane.

3.3 Low-friction modeling

In this work, low-friction is modeled by adopting an SHS model based on the slip length: a case of Robin boundary condition in which tangential velocity on the wall \mathbf{u}_s is proportional to the derivative of the fluid velocity in the normal direction to the wall, as described in Eq. (8).

$$\mathbf{u}_s = b \frac{\partial \mathbf{u}}{\partial \mathbf{n}}, \quad (8)$$

in which \mathbf{u}_s is wall surface velocity; b , the slip length, assumed to be constant; $\partial \mathbf{u} / \partial \mathbf{n}$, gradient of velocity in the normal-surface direction.

Figure 6 shows the schematics of flow velocity profile over an SHS. The fluid has a superficial velocity of $u_s = u(0) \neq 0$, appearing to slip over the surface.

The slip length is a well-established model to simplify the SHS behavior, being used in several works, such as Min and Kim (2004), Daniello et al (2009) or Seo and Mani (2016). This model has been used in this work to model the SHS effect

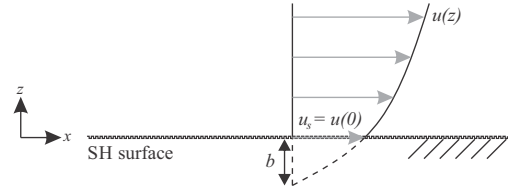


Fig. 6 Schematic of apparent velocity profile due to SHS. Adapted from Ou et al (2004).

without concerning about the microscopic effect nor dealing with water surface tension and the air pockets. It is not the scope of this work to study the effects of molecular dynamics of hydrophobia.

3.4 Mesh overview

The desired meshes have the following characteristics: y^+ close to 1.0; represent the rounded geometry of the propeller tip; and have an acceptable quality of the mesh, especially in terms of element aspect ratio and growing rate. Equation (9) defines the non-dimensional number y^+ :

$$y^+ = \frac{\rho U^* y}{\mu}, \quad (9)$$

in which, $U^* = \sqrt{\|\boldsymbol{\tau}\|/\rho}$ is the shear velocity; μ , dynamic viscosity; and y , distance from the wall to the mesh.

Meshes have four volumes of refinement control, shown in Fig. 7. The first two volumes, in blue and yellow, are refinements due to propeller wake. The third one, in red, is composed of a hollow cylinder and a cylinder after the hub, being used to refine the region of vortex detachment generated mainly in the propeller tip. The last one, in green, is a twisted cylinder that follows the propeller edge, to model the tip flow and eddy detachment. This refinement changes smoothly the first element of the boundary layer, in order to maintain y^+ near to 1.0.

The same hexahedral mesh used in previous works (Katsuno and Dantas, 2017, 2022) is adopted for the CFD analysis and to verify the TOM results. Katsuno and Dantas (2022), using the same mesh density and refinement volumes on the same propeller, compares the numerical results with experiments, showing also grid refinement studies to estimate the numerical uncertainties.

Despite the choice for the hexahedral type for CFD verification, a second mesh, polyhedral, is chosen to be used in the optimization framework,

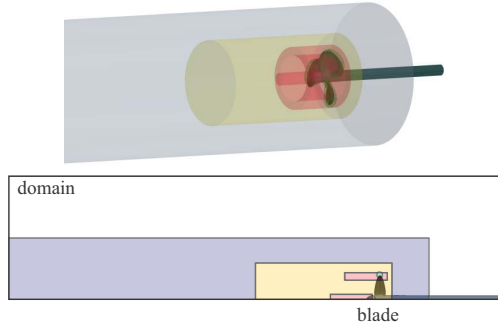


Fig. 7 Geometry of refinements (showing the complete propeller for better illustration purposes. The actual model consists of 1/3 of propeller) (top); section view (bottom).

Table 1 Comparative between volumetric meshes.

Name	Polyhedral	Hexahedral
Number of elements	8.39×10^5	3.71×10^6
Elements on blade	3.69×10^4	9.61×10^4
Acceptable volume change	100%	99.997%
Acceptable element quality	100%	100%

following the STAR-CCM+ recommendations for adjoint solver (Siemens, 2018). Moreover, it is easier to ensure good quality with few elements when a polyhedral mesh is adopted. The face of the polyhedral mesh in contact with the blade is adopted as the optimization mesh. Therefore, the elements in which the optimization can change the design variables are the same as the faces of the volumetric mesh elements that contact the propeller blade. Comparing the chosen hexahedral and polyhedral meshes, Tab. 1 indicates some particular comparatives.

Figure 8 compares the elements on the blade and Fig. 9, the volume of elements, which is possible to observe the effect of the volumes of refinement control on the element sizes.

Figure 10 shows that the rounded tip feature is represented on both meshes. There is attention that the last elements of prism layer dimensions are similar to its adjacent elements, ensuring good volume growth. For this, the scalar value element volume change, which describes the ratio between the element volume and its largest adjacent one, was observed. The value of 1.0 indicates an element that has the same volume as its adjacent one, and it is the ideal value. According to the software developer, values below 0.01 indicate bad elements.

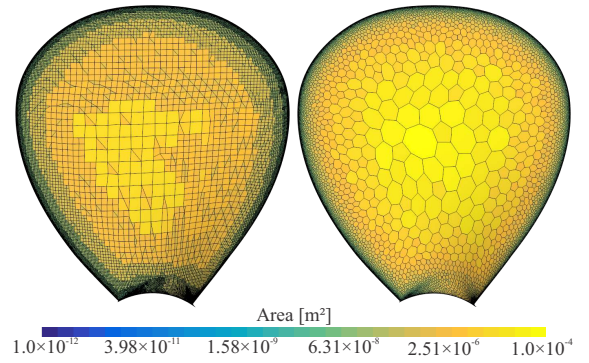


Fig. 8 Comparative between hexahedral (left) and polyhedral (right) meshes on the propeller blade, showing the face of the volumetric mesh elements. The right figure also represents the optimization mesh.

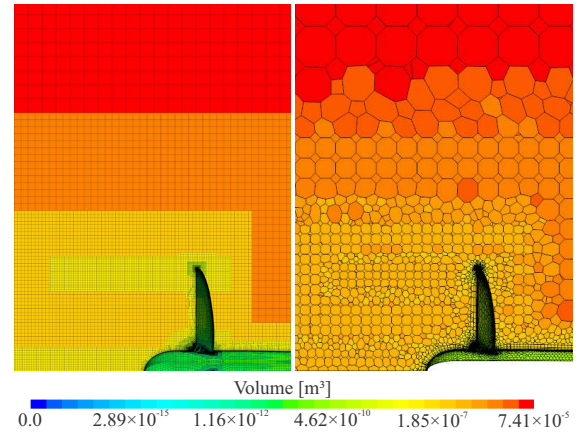


Fig. 9 Comparative of element volumes between hexahedral (left) and polyhedral (right) meshes.

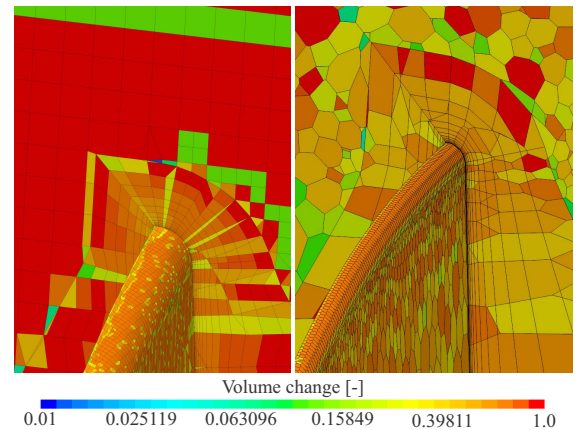


Fig. 10 Detail of mesh at propeller tip for the hexahedral (left) and polyhedral (right) meshes.

Section 3.6 compares the obtained results from each mesh.

3.5 Physical model and numerical setup

Simulations are conducted in a steady-state model, using the Reynolds-averaged Navier-Stokes (RANS) equations with the $k - \omega$ SST turbulence model (Menter, 1994). Segregated flow model is adopted for the hexahedral mesh, following the same numerical setup used in previous works (Katsuno and Dantas, 2017, 2022). Couple flow model is adopted for the primal and adjoint solvers in the optimization framework, following the recommendation of Siemens (2018). In both approaches, it is used second-order convection scheme for RANS and SST transport equations.

The segregated solver uses less memory (Siemens, 2018) and is used as the primary method for this work. Coupled solver has the advantage of robustness for solving flows with dominant source terms, such as rotation, and is used for optimization problems, since the adjoint module is available with the coupled solver.

Water is considered incompressible, density is 998.16 kg/m^3 and the dynamic viscosity, $1.0016 \times 10^{-3} \text{ Pa}\cdot\text{s}$. Turbulence intensity is set to 1%, the same value measured at the IPT (Institute for Technological Research) Cavitation Tunnel using particle image velocimetry in the condition without the propeller. Turbulent length scale is set as 0.005 m, 7% of characteristic length, defined as the chord on the 70% of propeller radius.

3.6 Segregated and coupled solvers comparison

In order to evaluate the performance of the candidate meshes, one operation condition is simulated at $J = 0.57$: advance velocity of 3.029 m/s and rotation velocity of 1608 RPM, without hydrophobic condition.

Fig. 11 shows the C_p distribution and Fig. 12, the C_f distribution.

Although it produces different values of hydrodynamic coefficients, note that the distribution is roughly similar in both cases of C_f and C_p .

The visual comparison is also conducted by using the Q-criterion, defined by:

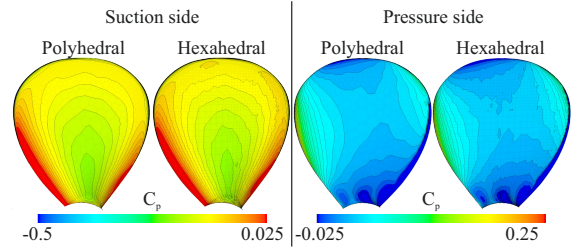


Fig. 11 Comparative of C_p between polyhedral and hexahedral meshes.

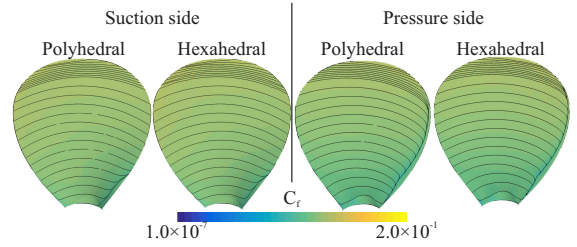


Fig. 12 Comparative of C_f between polyhedral and hexahedral meshes.

$$Q_{\text{crit}} = \frac{1}{2} \left(\|\boldsymbol{\Omega}\|^2 - \|\mathbf{D}\|^2 \right), \quad (10)$$

in which $\boldsymbol{\Omega}$ is the vorticity tensor. In other words, Q-criterion highlights vorticities that have small deformation (Jeong and Hussain, 1995). In this sense, boundary layer regions are penalized by the Q-criterion.

Figure 13 shows the Q-criterion iso-surface in the hexahedral and polyhedral meshes. Presenting larger elements, the polyhedral mesh dissipates the vorticity generated by the propeller in a shorter distance, when compared to the hexahedral mesh, being perceptible by the length of the iso-surface.

It is concluded that using the polyhedral mesh into the optimization framework is acceptable since the distribution of C_p and C_f are reasonably similar to the results from the hexahedral mesh, so it should lead to a similar optimized design. Subsequently, the topology of SHS distribution must be mapped to the hexahedral mesh in order to obtain the hydrodynamic coefficients in the same numerical model that was previously compared with experiments, allowing a fair comparison in other conditions.

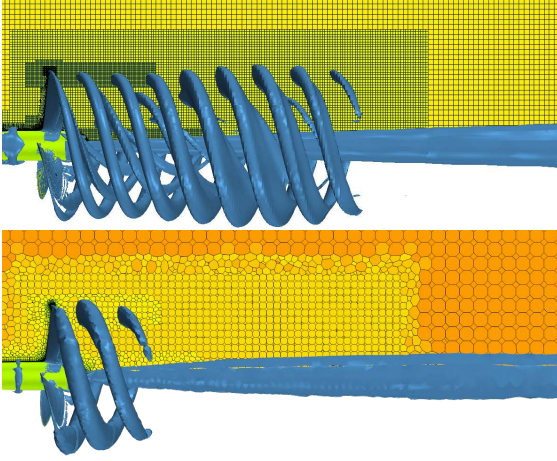


Fig. 13 Q-criterion iso-surface of 200 s^{-2} using the hexahedral (top) and polyhedral (bottom) meshes.

4 Optimization formulation

4.1 Material model and surface constraint

From a Topology Optimization point of view, the hydrophobic level is represented by the slip length value within the range $[0; \bar{b}]$. Pseudo-density $\hat{\rho}$ is a function from 0.0 to 1.0 that correlates the range of slip length $[0; \bar{b}]$. Thus, zero pseudo-density results in $b = 0$ and pseudo-density of 1.0 results in $b = \bar{b}$.

It is required to penalize intermediate values to allow an interpretation: although it is possible to have a surface covered by several slip lengths, it is studied the application of a painting that imposes a super-hydrophobic behavior. This painting is assumed to apply the same value of slip length. In this sense, it is important to have extremized values of $\hat{\rho}$, which can be interpreted in the real world as to where to apply or not the painting.

Based on Rozvany et al (1992), which proposes the solid isotropic material with penalization (SIMP) model, the following material model is defined with a penalization factor q in the pseudo-density to avoid intermediate values:

$$b(\hat{\rho}) = \bar{b} \hat{\rho}^q. \quad (11)$$

The partial derivative of slip length with respect to (w.r.t.) the pseudo-density is:

$$\frac{\partial b}{\partial \hat{\rho}} = \bar{b} q \hat{\rho}^{q-1}. \quad (12)$$

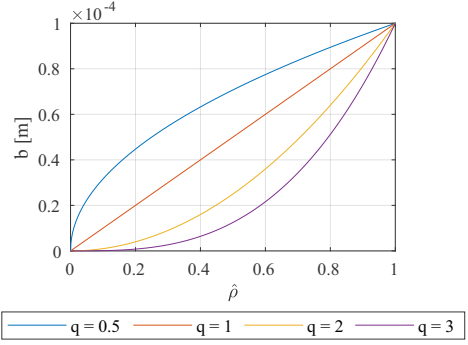


Fig. 14 SIMP-based model example for $\bar{b} = 1 \times 10^{-4} \text{ m}$ and several penalization factors q .

It is possible to observe the effect of penalization w.r.t. values of pseudo-densities in Fig. 14. This penalization bias intermediate values for some extreme values of b .

Another approach that extremizes values of pseudo-density $\hat{\rho}$ is to restrict the sum of $\hat{\rho}$ in the design domain. This procedure is done in several fluid topology optimization works, as described in Bendsoe and Kikuchi (1988) and applied in Gersborg-Hansen et al (2005); Pingen and Maute (2010); Romero and Silva (2014); Dilgen et al (2018). The formulation for the surface-average value of pseudo-density is:

$$\hat{g} = \frac{\int_{\Theta} \hat{\rho} dA}{\int_{\Theta} dA} \xrightarrow{\text{discret}} \frac{\sum_f \hat{\rho} A_f}{\sum_f A_f}, \quad (13)$$

in which Θ is the design surface, and the subscript f , discretized faces of Θ .

4.2 Low-friction implementation

The boundary condition for modeling hydrophobicity is not natively implemented in the CFD software. The tangential velocity can not be directly determined, since using Eq. (8) changes the shear stress, which leads to a different tangential velocity, requiring an iterative process. Because of this, an artifact is made to impose a wall with tangential velocity based on Eq. (8): to obtain convergence, the equation had to be relaxed. Also, based on the proposed SIMP-based model in Eq. (11), the numerical implementation of the boundary condition for the tangential velocity on the propeller blade considering the pseudo-density is:

$$\mathbf{u}[i] = a \left(\bar{b} \hat{\rho}^q \frac{\partial \mathbf{u}[i]}{\partial \mathbf{n}} \right) + (1-a) \langle \mathbf{u}[i \dots i-5] \rangle. \quad (14)$$

in which $\mathbf{u}[i]$ is the imposed boundary condition of tangential velocity; a , an under-relaxation factor and $\langle \mathbf{u}[i \dots i-5] \rangle$ is the mean value of \mathbf{u} in the last 5 iterations. SHS in simulation is set as wall boundary condition, so the turbulent boundary layer of the $k-\omega$ SST is still modeled. It is noted that hydrophobic simulations are more unstable than conventional ones. The convergence is obtained with low values of under-relaxation factor (e.g.: for simulations with $\bar{b} = 1 \times 10^{-3}$ m, an under-relaxation factor of $a = 6 \times 10^{-4}$ was adopted), which requires more iterations than usual simulations without SHS to obtain a general convergence.

4.3 Cost function formulation

The cost function is the maximization of propeller efficiency η_0 , Eq. (1). To obtain the partial derivative of propeller efficiency w.r.t. slip length, consider the cost function C :

$$C = \eta_0 = \frac{T v_a}{2\pi n Q}. \quad (15)$$

In Eq. (15), only T and Q are dependent of b . Other variables are assumed as constants. The adopted numerical model (see Sec. 3.5) calculates T and Q as:

$$T = \sum_{\Theta} \left[(p\mathbf{I} - 2(\mu + \mu_t)\mathbf{D}) \cdot \mathbf{s} \right] \cdot \mathbf{e}_a, \quad (16)$$

$$Q = \sum_{\Theta} \left[\mathbf{r} \times (p\mathbf{I} - 2(\mu + \mu_t)\mathbf{D}) \cdot \mathbf{s} \right] \cdot \mathbf{e}_a, \quad (17)$$

in which \mathbf{e}_a is the unit vector aligned with advance velocity (and propeller axis); and \mathbf{r} , distance vector between the propeller axis and the element location.

To solve the gradient of the strain rate tensor \mathbf{D} on a wall for the presented problem, Siemens (2018) describes the numerical implementation, which is also differentiated and explained in details in Katsuno et al (2020). Close to the wall, the turbulence kinetic energy is close to zero,

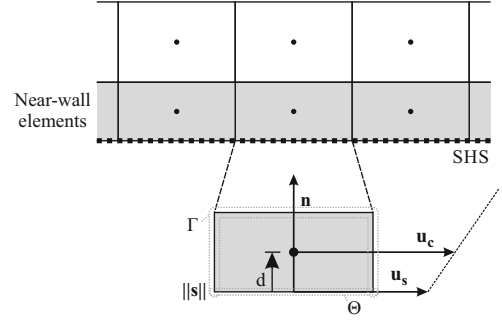


Fig. 15 Schema of near-wall elements and the velocities.

and consequently, the turbulent viscosity ratio is also close to zero, allowing the approximation $\mu + \mu_t \approx \mu$. Considering a representation of a mesh element that contacts with the design surface, as shown in Fig. 15, the numerical expression to solve the dot product of \mathbf{D} and \mathbf{s} can be written as:

$$\sum_{\Theta} 2\mu \mathbf{D} \cdot \mathbf{s} \Rightarrow \sum_{\Theta} \mu \frac{\partial \mathbf{u}}{\partial \mathbf{n}} \|\mathbf{s}\| \Rightarrow \mu \frac{\mathbf{u}_c - \mathbf{u}_s}{d} \|\mathbf{s}\|, \quad (18)$$

in which \mathbf{u}_c is the velocity at cell center; d , distance vector between the face and cell center; and \mathbf{u}_s , velocity on the face (given by Eq. (8) for SHS). Therefore, considering the pseudo-density, \mathbf{u}_s can be written as:

$$\mathbf{u}_s = b \frac{\partial \mathbf{u}}{\partial \mathbf{n}} = b \frac{\tau}{\mu} = \bar{b} \hat{\rho}^q \frac{\tau}{\mu}. \quad (19)$$

4.4 Discrete adjoint formulation

Consider a system of partial differential equation (PDE) given by Eq. (20), in which \mathbf{q} is the output of PDE solution (in this case, \mathbf{q} is an array with pressure and velocities that satisfies Navier-Stokes equations). The vector \mathbf{f} is composed by the Continuity f_c (given by Eq. (3)), and Navier-Stokes residuals \mathbf{f}_m (given by Eq. (4)). Therefore:

$$\mathbf{f}(\mathbf{q}(\hat{\rho}), \hat{\rho}) = \begin{bmatrix} f_c \\ \mathbf{f}_m \end{bmatrix} = 0. \quad (20)$$

Consider a cost function $C(\mathbf{q}(\hat{\rho}), \hat{\rho})$ with the same input parameters. By deriving the cost function and applying the chain rule:

$$\frac{dC}{d\hat{\rho}} = \frac{\partial C}{\partial \mathbf{q}} \frac{d\mathbf{q}}{d\hat{\rho}} + \frac{\partial C}{\partial \hat{\rho}}. \quad (21)$$

The $\partial C / \partial \hat{\rho}$ term in Eq. (21) can be easily determined since the cost function expression is

well-defined. The difficulty consists in obtaining the implicit part, which is obtained by deriving the system of PDE in Eq. (20) with the chain rule:

$$\frac{d\mathbf{f}}{d\hat{\rho}} = \frac{\partial \mathbf{f}}{\partial \mathbf{q}} \frac{d\mathbf{q}}{d\hat{\rho}} + \frac{\partial \mathbf{f}}{\partial \hat{\rho}} = 0. \quad (22)$$

Rearranging the terms:

$$\frac{d\mathbf{q}}{d\hat{\rho}} = - \left(\frac{\partial \mathbf{f}}{\partial \mathbf{q}} \right)^{-1} \frac{\partial \mathbf{f}}{\partial \hat{\rho}}. \quad (23)$$

The adjoint vector $\boldsymbol{\lambda}$ is defined by inserting the obtained expression into Eq. (21):

$$\frac{dC}{d\hat{\rho}} = - \underbrace{\frac{\partial C}{\partial \mathbf{q}} \left(\frac{\partial \mathbf{f}}{\partial \mathbf{q}} \right)^{-1} \frac{\partial \mathbf{f}}{\partial \hat{\rho}}}_{\boldsymbol{\lambda}} + \frac{\partial C}{\partial \hat{\rho}}. \quad (24)$$

Finally, the sensitivity of the cost function C w.r.t. $\hat{\rho}$ is:

$$\frac{dC}{d\hat{\rho}} = -\boldsymbol{\lambda} \cdot \frac{\partial \mathbf{f}}{\partial \hat{\rho}} + \frac{\partial C}{\partial \hat{\rho}}. \quad (25)$$

In this work, the pseudo-density $\hat{\rho}$ is related to the slip length b , as expressed in Eq. (11). Therefore, Eq. (25) can be rewritten to consider this relation:

$$\frac{dC}{d\hat{\rho}} = -\boldsymbol{\lambda} \cdot \frac{\partial \mathbf{f}}{\partial b} \frac{\partial b}{\partial \hat{\rho}} + \frac{\partial C}{\partial b} \frac{\partial b}{\partial \hat{\rho}}. \quad (26)$$

The adjoint solution vector $\boldsymbol{\lambda}$ is obtained using the adjoint flow solver. More details on the numerical approach of how to obtain the adjoint vector with feasible computational cost are described in [Siemens \(2018\)](#).

To obtain the derivative of residuals with respect to slip length $\partial \mathbf{f} / \partial b$, consider the mesh element representation shown in Fig. 15. This element, with volume Ω , is formed with two surface groups: Θ , in full contact with a design surface (in which can be an SHS); and Γ , the remaining surfaces, that are in contact with other mesh elements. By applying the Continuity, Eq. (3), and Navier-Stokes equations, Eq. (4), in this near-wall element:

$$f_c = \int_{\Gamma} \mathbf{u}_{\mathbf{r}} \cdot d\mathbf{s} + \int_{\Theta} \mathbf{u}_{\mathbf{r}} \cdot d\mathbf{s}, \quad (27)$$

$$\begin{aligned} \mathbf{f}_{\mathbf{m}} = & \int \rho \boldsymbol{\omega} \times \mathbf{u} d\Omega + \int_{\Gamma} \rho \mathbf{u} \otimes \mathbf{u}_{\mathbf{r}} \cdot d\mathbf{s} \\ & + \int_{\Theta} \rho \mathbf{u} \otimes \mathbf{u}_{\mathbf{r}} \cdot d\mathbf{s} + \int_{\Gamma} p \mathbf{I} \cdot d\mathbf{s} \\ & + \int_{\Theta} p \mathbf{I} \cdot d\mathbf{s} - \int_{\Gamma} 2(\mu + \mu_t) \mathbf{D} \cdot d\mathbf{s} \\ & - \int_{\Theta} 2(\mu + \mu_t) \mathbf{D} \cdot d\mathbf{s}. \end{aligned} \quad (28)$$

Note that only Θ surface has a dependency of b in the formulation. Also, even though it is an SHS, the impermeability condition is maintained. So, the convective term in Θ is zero. Thus, to emphasize terms that has b dependency, f_c and $\mathbf{f}_{\mathbf{m}}$ equations are reduced to:

$$f_c = [\dots], \quad (29)$$

$$\mathbf{f}_{\mathbf{m}} = - \int_{\Theta} 2(\mu + \mu_t) \mathbf{D} \cdot d\mathbf{s} + [\dots]. \quad (30)$$

In other words, f_c has no explicit dependency of b . It implies that only $\mathbf{f}_{\mathbf{m}}$ influences the implicit part of sensitivity calculation. Considering the numerical expression of the strain rate tensor for SHS in Eq. (18), and the $\mathbf{u}_{\mathbf{s}}$ expression in Eq. (19), the derivative yields:

$$\frac{\partial \mathbf{f}}{\partial b} = \begin{bmatrix} 0 \\ \frac{A}{d} \boldsymbol{\tau} \end{bmatrix}. \quad (31)$$

To obtain the derivative of the cost function with respect to slip length $\partial C / \partial b$, the quotient rule is applied:

$$\frac{\partial C}{\partial b} = \frac{v_a}{2\pi n Q^2} \left(Q \frac{\partial T}{\partial b} - T \frac{\partial Q}{\partial b} \right). \quad (32)$$

The derivative of thrust and torque can be obtained based on the differentiated expression of strain rate tensor for SHS, Eq. (18) and Eq.(19):

$$\frac{\partial T}{\partial b} = -\frac{A}{d} \boldsymbol{\tau} \cdot \mathbf{e}_{\mathbf{a}}, \quad (33)$$

$$\frac{\partial Q}{\partial b} = \left(\mathbf{r} \times -\frac{A}{d} \boldsymbol{\tau} \right) \cdot \mathbf{e}_{\mathbf{a}}. \quad (34)$$

4.5 Summary of the optimization formulation

In this work, the objective is to increase the hydrodynamic efficiency of a marine propeller η_0 at a

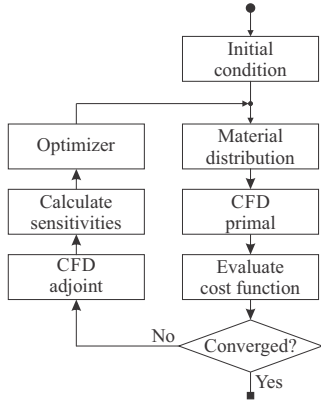


Fig. 16 Topology optimization flowchart.

defined advance ratio. For a standard commercial ship, in general, the propeller is designed specifically for one operating condition, as most of the ship's operation time is carried sailing at a single speed. Therefore, the optimization problem focuses only on one operating condition, $J = 0.7$ and $n = 1600$ RPM, which is a condition close to the maximum hydrodynamic efficiency.

The formal formulation of the optimization problem is defined in Eq. (35):

$$\begin{array}{ll}
 \text{Max}_{\hat{\rho}} & C = \eta_0 \\
 \text{such that} & \hat{g}(\hat{\rho}) = \frac{\int_{\Theta} \hat{\rho} dA}{\int_{\Theta} dA} \leq \hat{g}^* \\
 & 0 \leq \hat{\rho} \leq 1
 \end{array} \quad (35)$$

in which C is the cost function and \hat{g}^* , surface average limit.

5 Numerical implementation

5.1 Optimization flowchart

The optimization flowchart is schematically described in Fig. 16.

The steps to run the optimization require first defining an initial material distribution. Then, the primal problem is solved using the CFD to get the hydrodynamics of the propeller under the SHS condition.

With the primal problem solved, the cost function and other properties can be evaluated. If the stopping criteria of the optimizer are not achieved, it is moved to the adjoint CFD simulation by using

the same polyhedral mesh as the primal problem. The primal solution is frozen, and the adjoint problem is conducted.

With the sensitivity information, the optimizer calculates the next design distribution of hydrophobic material. The process is repeated until it reaches the convergence criteria.

5.2 Optimizer, primal and adjoint solver

This work uses the Interior Point Optimizer (IPOPT) package (Wächter and Biegler, 2006), which is an internal point optimization algorithm. The IPOPT software applies a primal-dual barrier method that solves a sequence of barrier problems. The complete procedure and mathematical background can be found in its reference.

The same CFD software for the primal and adjoint solver, STAR-CCM+ 13 with double-precision, is chosen, avoiding the need for external communications between two different software and extensive data exchange from a typically large number of elements from CFD simulation. STAR-CCM+ contains the pre-processing, solver, and post-processing tools in the same environment, including the adjoint module if the primal problem is solved using the coupled-flow approach. However, the problem can be adapted without further modifications to any software, especially if it has an adjoint module.

6 Results of hydrophobic simulations

With a defined method for propeller simulation, a numerical analysis based on RANS CFD software is done to study the behavior of the boundary layer flow with the condition that imposes the low-friction / hydrophobic effect in a fully-covered super-hydrophobic propeller (Katsuno et al, 2018). This section aims to estimate the gain of performance in propellers, guiding the definitions and restrictions that should be looked for the topology optimization. The simulations are carried out with the hexahedral mesh at a rotational speed of $n = 1600$ RPM.

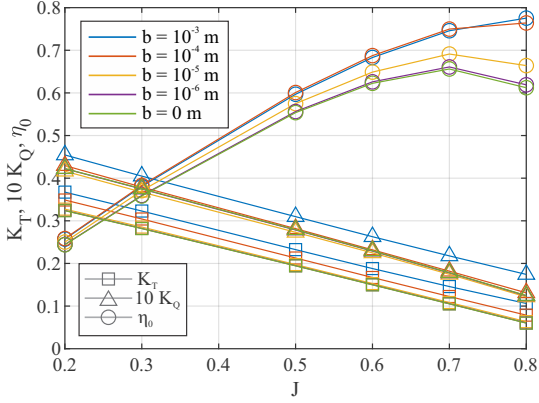


Fig. 17 Open water diagram with hydrophobic painting fully covering the blades.

6.1 Open water diagram

Figure 17 shows the open water diagram, presenting thrust, torque, and the hydrodynamic efficiency for several slip lengths and advance ratios.

It is observed a gain in efficiency, especially for values above $b = 1 \times 10^{-6}$ m and not significant gains for values above $b = 1 \times 10^{-4}$ m. These results are due to the increase in K_Q , slowing the efficiency gain.

To further study these conditions, two operating conditions are analyzed in more detail: low ($J = 0.3$) and high ($J = 0.7$) advance ratios.

6.2 Skin friction and pressure coefficient analysis

Figure 18 shows the streamlines of skin friction coefficient on the suction and pressure sides for $J = 0.3$; and Fig. 19, for $J = 0.7$. A detachment in the streamlines is noted as the hydrophobicity increases, especially in the upper region of the propeller on both suction and pressure sides.

Figure 20 shows the pressure coefficient distribution on the suction and pressure side for $J = 0.3$. An increase in suction can be noted as the effect of hydrophobicity increases, especially in the upper region of the propeller.

Figure 21 shows the pressure coefficient distribution for $J = 0.7$. It is noted an increase in suction and pressure in regions close to the trailing edge.

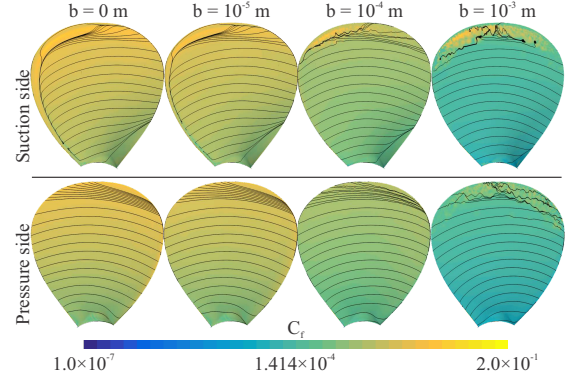


Fig. 18 Skin-friction coefficient C_f , varying slip length b , for $J = 0.3$.

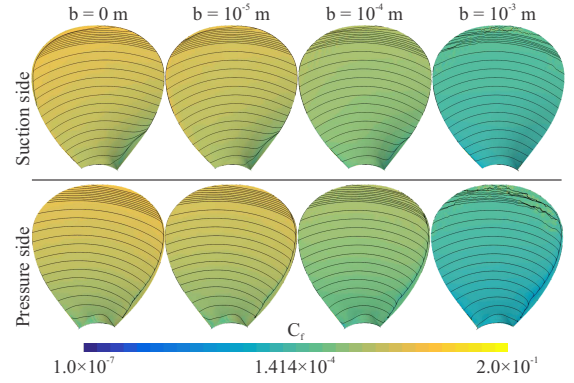


Fig. 19 Skin-friction coefficient C_f , varying slip length b , for $J = 0.7$.

6.3 Propeller efficiency - C_p trade-off

It can be observed from Fig. 17 that efficiency does not appear to significant increase from $b = 1 \times 10^{-4}$ m to $b = 1 \times 10^{-3}$ m. However, observing Fig. 20 and Fig. 21, there is an increase in the suction pressure for these values of b . It motivates to analyze the trade-off between the skin-friction drag reduction due to SHS presence, an expected result, and the increase of suction pressure (reduction of absolute pressure), which is important as it may lead to cavitation inception. An analysis with intermediate values of b are performed ($b = 1 \times 10^{-6}$, 1×10^{-5} , 8×10^{-5} , 1×10^{-4} , 2×10^{-4} , 4×10^{-4} , 6×10^{-4} , 8×10^{-4} , and 1×10^{-3} m). The values are compared in terms of propeller efficiency η_0 and surface fraction of blade suction-side that presents C_p less than -0.2 , named p_{C_p} . Two advance ratio are studied, $J = 0.3$ and $J = 0.7$. The results are shown in Fig. 22.

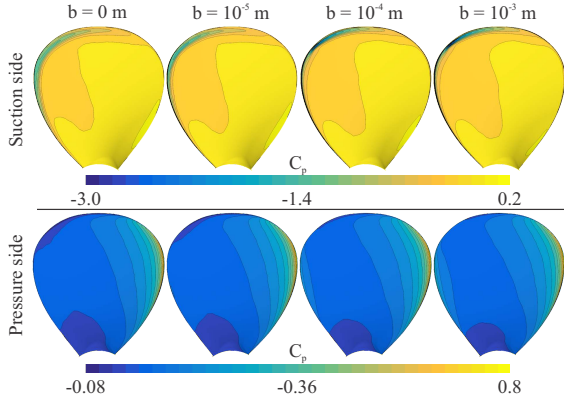


Fig. 20 Pressure coefficient C_p , varying slip length b , for $J = 0.3$.

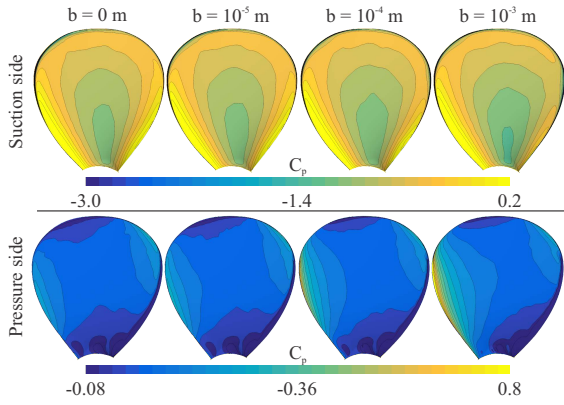


Fig. 21 Pressure coefficient C_p , varying slip length b , for $J = 0.7$.

It can be noted that in both J cases there is not a strictly increase relationship of propeller efficiency and p_{C_p} fraction, even for $J = 0.7$, in which this fraction is below 10%. Therefore, with the assumptions made for modeling the SHS over a propeller, it can conclude with the preliminary results that high values of b are not recommended, once there is a limit of efficiency gain and higher values induce a higher surface fraction of low C_p . The results motivated the approach to apply the TOM to determine regions of the propeller surface that must turn to an SHS to improve a given cost function and observe its limits.

7 Topology optimization of painting distribution

This section applies TOM to increase the hydrodynamic efficiency of the propeller by defining

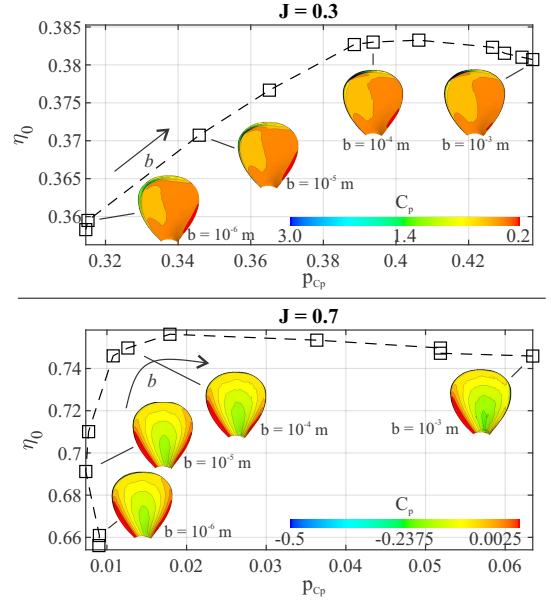


Fig. 22 Hydrodynamic efficiency η_0 in function of the fraction of suction side with $C_p < -0.2$, named p_{C_p} , for $J = 0.3$ (top) and $J = 0.7$ (bottom); and scalar figures of the C_p distribution on the suction face.

SHS regions on the blade, in which the maximum amount of paint is limited.

The topology optimization results are presented and discussed. As part of the procedure, the results are post-processed to get paint distribution. Since the adopted mesh is designed to be used only inside the optimization framework, the topology solution is transposed to the hexahedral mesh. Finally, the results are compared with no-SHS and full-SHS conditions, with the hexahedral mesh.

7.1 Optimization of SHS distribution

Katsuno et al (2020) observed that the maximum slip length \bar{b} does not significantly change the topology of SHS distribution. Thus, it is expected not having an exact value of \bar{b} does not significantly impact the obtained topology from optimization. It is chosen the $\bar{b} = 1 \times 10^{-4}$ m and penalization $q = 4.0$. Three optimizations are conducted changing the value of \hat{g}^* . The initial condition is $\hat{\rho} = 0.1$ in whole surface. Figure 23 shows the optimization process along the iterations, showing the cost function η_0 and the constraint \hat{g} for $\hat{g}^* = 0.3, 0.5, 0.7$.

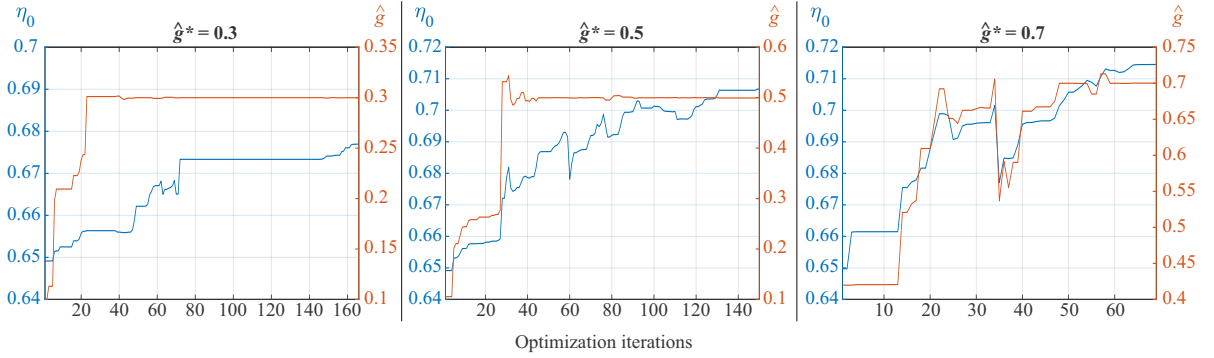


Fig. 23 Propeller efficiency η_0 and surface-average value of pseudo-density \hat{g} along with optimization iterations for $\hat{g}^* = 0.3, 0.5$, and 0.7 .

The results must be post-processed in order to indicate which regions should be covered with super-hydrophobic painting. This post-processing is done by applying a filter-like process: all values of pseudo-density above a threshold are equal to one and all below are equal to zero. The threshold is chosen such that it still satisfies the surface constraint \hat{g} . Figure 24, Fig. 25 and Fig. 26 show topology optimization solutions and the post-processing results after treatment procedures for cases of $\hat{g}^* = 0.3, 0.5, 0.7$, respectively. The obtained value of the threshold is around 0.5 for all cases, which was expected as it was adopted the SIMP-based material with a penalization of $q = 4.0$.

7.2 Hexahedral mesh comparison

The post-processed topology obtained after optimization is mapped to the hexahedral mesh using nearest-neighbor (closest point) interpolation from cell-centered data of polyhedral mesh topology. Getting hydrodynamic performance values using the same hexahedral mesh makes it possible to perform a fair comparison of the gain of hydrodynamic efficiency between a propeller without any SHS, with topology optimized and full-SHS. Figure 27 shows the post-processed topology using the polyhedral mesh and the mapping result on the hexahedral mesh.

7.3 Comparative with no-SHS and full-SHS

Finally, from the mapped topology solution, the results can be compared with no-SHS and full-SHS conditions using the same hexahedral mesh.

Figure 28 shows the hydrodynamic efficiency comparison.

The general topologies obtained from the optimization process are regions covered at the propeller tip and extending toward the center. It is also possible to observe the presence of SHS, in smaller quantities, in the region close to the axis. Also, it can be observed that the starting radius of the painting is different between suction and pressure surfaces. These results also endorse the choice of topology optimization, since such generality of design would be very complicated in other types of optimization methods.

Using a simple post-processing approach that adopts a threshold value to interpret elements with and without SHS painting could generate some jaggy results, as observed in the topology of the suction side of $\hat{g}^* = 0.3$ case, especially on the center of the painted area, which is not pronounced in the other cases. The results suggest a tendency of painting the top edge of the propeller and some parts above the central region of the blade. Observing the results of $J = 0.7$ in Fig. 19, it is possible to notice some noisy streamlines close to the top of the propeller as the slip length increases, which may indicate a possible region with flow separation and instability in this region. Based on the results of flow separation observed in previous papers (see, for example, Fig. 30 in Katsuno et al (2020)), it is concluded that the optimizer avoids filling with SHS regions that may present some adverse pressure gradient (which leads to the flow separation and recirculation) because it may increase drag. Being close to the edge of the propeller, a region with high

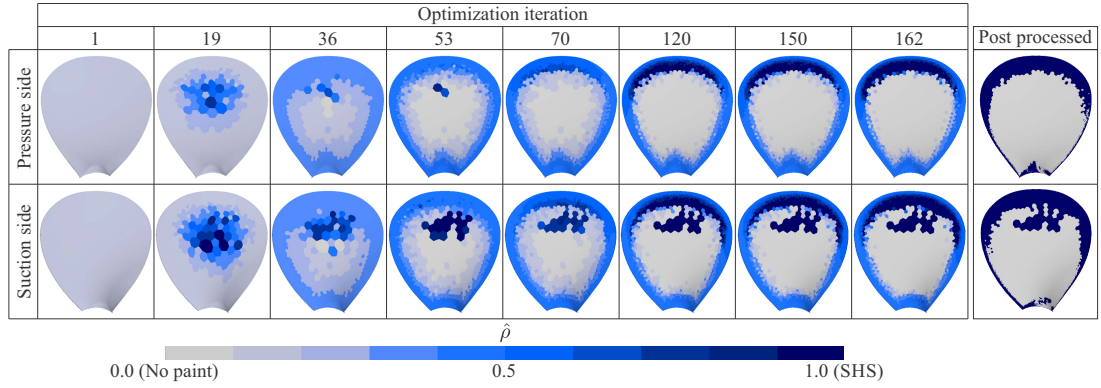


Fig. 24 Topology evolution along optimization iterations for $\hat{g}^* = 0.3$.

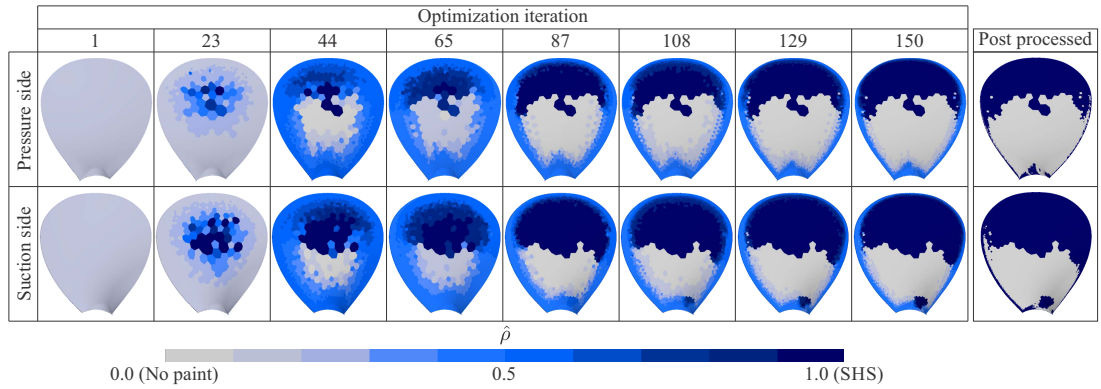


Fig. 25 Topology evolution along optimization iterations for $\hat{g}^* = 0.5$.

vorticity may expect to have some flow separation. Adding this effect to the optimization mesh discretization, which is coarser in the blade center, helps to explain this behavior in the results. Yet, even with the jaggy topology, the results are helpful to indicate which regions to prioritize SHS painting, being possible to have smoother results with a different post-processing procedure.

As stated, the objective of this work does not intend to investigate the modeling or practical manufacture of SHS, but to use a well-known model and apply it to a topology optimization problem in a turbulent flow. Because of this, it is chosen to impose a paint constraint to understand which regions should be prioritized. In this way, it is possible to observe the growth of regions in which the optimizer chooses to prioritize, showing where are the critical regions on the blade. By studying three cases by varying the surface constraint, it is observed that, for this propeller, the

tip should be prioritized and, in smaller quantities, regions near the axis.

In this problem, the cost function is defined as being only the hydrodynamic efficiency. If it would be considered other factors, such as the cost of painting, a maximum trade-off point could appear without a painting limitation. Methods for creating an SHS can vary from a sprayable painting to a corrosion-controlled process on a propeller surface to create micro-surface elevations and traps small air pockets. In any case, it is reasonable to consider that the cost of creating an SHS is proportional to the area. As this linear function would be well-defined, obtaining the value and its derivative would be easy to be implemented. Other improvements on the cost function could be including the consequences of increasing the propeller efficiency, such take into account the price of engine fuel.

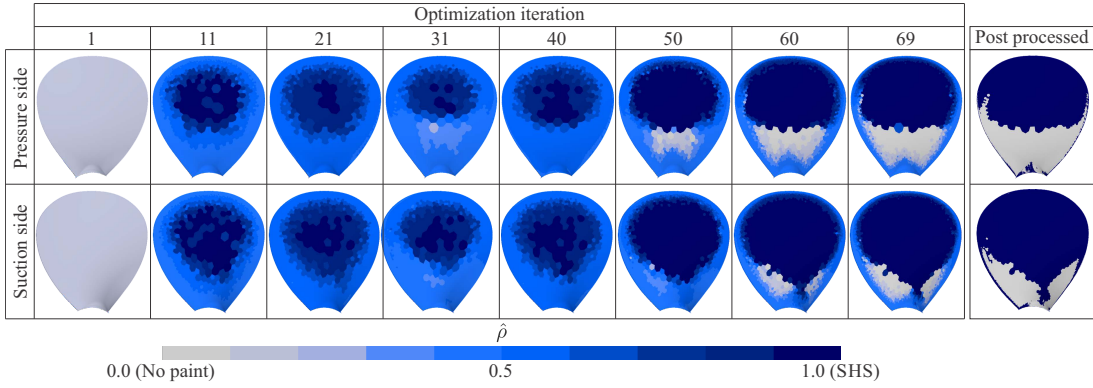


Fig. 26 Topology evolution along optimization iterations for $\hat{g}^* = 0.7$.

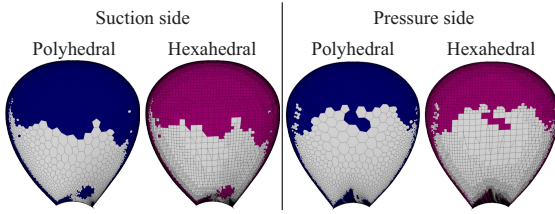


Fig. 27 Mapping results from polyhedral and hexahedral meshes, for $\hat{g}^* = 0.5$.

8 Conclusions

This work presented the study of the hydrodynamic implication of the low-friction painting in a marine propeller. It is focused on the consequences on the hydrodynamic performance, whereas the hydrodynamic of the low-friction was simplified by the slip length model. Results with propeller showed that an increase in slip length is not always followed by an increase in the hydrodynamic efficiency, presenting an efficiency gain limit. From this limit, the efficiency no longer increases with hydrophobicity, but the area of low pressure continues to grow. In the propeller topology optimization study, three surface constraint cases are performed. For this propeller, a tendency can be observed to prioritize the distribution of SHS on the propeller tip and, in a smaller quantity, on regions near the axis. Also, the suction surface is prioritized over the pressure surface.

It is expected that this work could stimulate future researches in this approach of the energy-saving devices, collaborating to the EEDI of ships, to the reduction of greenhouse gases, and promoting a more sustainable future. The development in this work, in which topology optimization on the surface is applied, can be extrapolated to other

applications. An example could be the roughness distribution, in order to change the transition point using a laminar-turbulent transitional model. Inducing a transition may be interesting to control the cavitation inception, even if the performance is degraded, which is critical for submarine applications, for example.

More details about the numerical model set-up and details of experimental campaign and tests of the propeller without SHS can also be found in [Katsuno \(2020\)](#). For future works, it is interesting to validate the super-hydrophobic model by comparing it with experimental results: for this, it recommends applying a super-hydrophobic treatment using a painting or some mechanical approach, since the turbulent condition of the propeller can be harsh for painting. The feasibility of conducting a controlled corrosion treatment to obtain a hydrophobic surface by electrolysis can be evaluated.

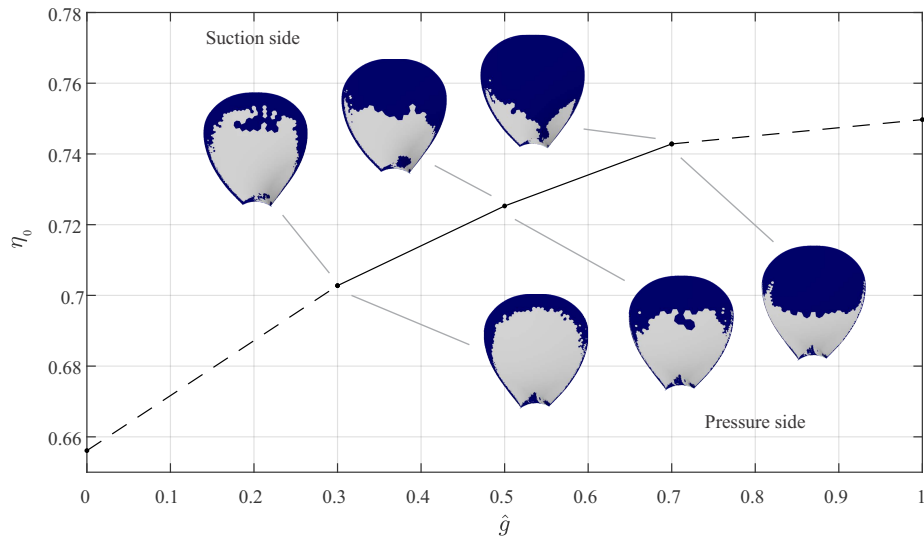


Fig. 28 Propeller efficiency η_0 in function of surface constrain adopted in optimization process and comparison with no-SHS ($\hat{g} = 0$) and full-SHS ($\hat{g} = 1$).

Acknowledgments. The authors thank Artur Lidtke and Prof. Fred van Keulen for their comments as committee members of the defense on which this work is based. The first and second authors thank the Institute for Technological Research (IPT) and the Foundation for the Institute for Technological Research (FIPT). The second author thanks the Brazilian Innovation Agency (FINEP), under grant CTInfra - 01.18.0082.01. The last author thanks the financial support of the Brazilian National Council for Scientific and Technological Development (CNPq), under grant 302658/2018-1.

Conflict of interest. The authors declare that they have no conflict of interest.

Replication of results. With the presented procedures, it is expected to be possible to apply the formulation in other CFD or optimizer software: Fig. 4 describes the dimensions and information on how to replicate the adopted propeller. Section 3.2 presents all the dimensions to recreate the domain for CFD simulations and the adopted boundary conditions. Section 3.4 describes all adopted volumes of refinement to obtain the same mesh topologies. Section 3.5 shows the CFD setup, as the value for some constants, such as the density and viscosity. Section 5 describes the optimization flowchart. The framework of communication between the CFD and the optimizer is the same as previous work, described in the

Replication of results section in Katsuno et al (2020).

References

- Bendsøe MP, Kikuchi N (1988) Generating optimal topologies in structural design using a homogenization method. *Computer Methods in Applied Mechanics and Engineering* 71(2):197–224. [https://doi.org/10.1016/0045-7825\(88\)90086-2](https://doi.org/10.1016/0045-7825(88)90086-2), URL <http://linkinghub.elsevier.com/retrieve/pii/0045782588900862>
- Borrvall T, Petersson J (2003) Topology optimization of fluids in Stokes flow. *International Journal for Numerical Methods in Fluids* 41(1):77–107. <https://doi.org/10.1002/fld.426>
- Cho SC, Hong YC, Cho SG, et al (2009) Surface modification of polyimide films, filter papers, and cotton clothes by HMDSO/toluene plasma at low pressure and its wettability. *Current Applied Physics* 9(6):1223–1226. <https://doi.org/10.1016/j.cap.2009.01.020>, URL <http://dx.doi.org/10.1016/j.cap.2009.01.020><http://linkinghub.elsevier.com/retrieve/pii/S1567173909000339>
- Daniello RJ, Waterhouse NE, Rothstein JP (2009) Drag reduction in turbulent flows over superhydrophobic surfaces. *Physics of Fluids* 21(8):085,103. <https://doi.org/10.1063/1.3207885>
- Dilgen CB, Dilgen SB, Fuhrman DR, et al (2018) Topology optimization of turbulent flows. *Computer Methods in Applied Mechanics and Engineering* 331:363–393. <https://doi.org/10.1016/j.cma.2017.11.029>
- Evgrafov A (2005) The Limits of Porous Materials in the Topology Optimization of Stokes Flows. *Applied Mathematics and Optimization* 52(3):263–277. <https://doi.org/10.1007/s00245-005-0828-z>
- Fu Y, Yuan C, Bai X (2017) A numerical study of drag reduction of superhydrophobic surfaces in shipping industry. In: 2017 4th International Conference on Transportation Information and Safety (ICTIS), vol 0.

- IEEE, pp 99–103, <https://doi.org/10.1109/ICTIS.2017.8047750>, URL <http://ieeexplore.ieee.org/document/8047750/>
- Gawn R, Burrill L (1957) Effect of cavitation On the Performance of a Series of 16-Inch Model Propellers. Insitution of Naval Architects
- Gersborg-Hansen A, Sigmund O, Haber R (2005) Topology optimization of channel flow problems. *Structural and Multidisciplinary Optimization* 30(3):181–192. <https://doi.org/10.1007/s00158-004-0508-7>
- International Maritime Organization (2015) IMO and Sustainable Development: How international shipping and the maritime community contribute to sustainable development. Tech. rep., URL <https://wwwcdn.imo.org/localresources/en/MediaCentre/HotTopics/Documents/IMOSDGBrochure.pdf>
- International Maritime Organization (2018) Initial IMO Strategy on Reduction of GHG Emissions from Ships. Tech. rep., URL https://wwwcdn.imo.org/localresources/en/OurWork/Environment/Documents/ResolutionMEPC.304%2872%29_E.pdf
- International Maritime Organization (2021) Fourth IMO Greenhouse Gas Study. Tech. Rep. 11, URL <https://wwwcdn.imo.org/localresources/en/OurWork/Environment/Documents/FourthIMOIGHGStudy2020-Fullreportandannexes.pdf>
- Jeong J, Hussain F (1995) On the identification of a vortex. *Journal of Fluid Mechanics* 285(-1):69. <https://doi.org/10.1017/S0022112095000462>
- Katsuno ET (2020) Topology optimization of the superficial painting pattern on model-scale propellers applied for hydrodynamic performance. Master’s thesis, Universidade de São Paulo, São Paulo, <https://doi.org/10.11606/D.3.2020.tde-06012020-122009>, URL <http://www.teses.usp.br/teses/disponiveis/3/3152/tde-06012020-122009/>
- Katsuno ET, Dantas JLD (2017) Analysis of the Blockage Effect on a Cavitation Tunnel Using CFD Tools. In: Volume 7B: Ocean Engineering. ASME, p V07BT06A043, <https://doi.org/10.1115/OMAE2017-61545>
- Katsuno ET, Dantas JLD (2022) Blockage effect influence on model-scale marine propeller performance and cavitation pattern. *Applied Ocean Research* 120:103,019. <https://doi.org/10.1016/j.apor.2021.103019>, URL <https://linkinghub.elsevier.com/retrieve/pii/S0141118721004788>
- Katsuno ET, Dozzi Dantas JL, Nelli Silva EC (2018) Analysis of Hydrophobic Painting in Model-Scale Marine Propeller. In: Volume 7B: Ocean Engineering. ASME, Madrid, p V07BT06A042, <https://doi.org/10.1115/OMAE2018-78209>
- Katsuno ET, Dantas JLD, Silva ECN (2020) Low-friction fluid flow surface design using topology optimization. *Structural and Multidisciplinary Optimization* 62(6):2915–2933. <https://doi.org/10.1007/s00158-020-02706-0>
- Korkut E, Atlar M (2012) An experimental investigation of the effect of foul release coating application on performance, noise and cavitation characteristics of marine propellers. *Ocean Engineering* 41(June):1–12. <https://doi.org/10.1016/j.oceaneng.2011.12.012>, URL <http://linkinghub.elsevier.com/retrieve/pii/S0029801811002873>
- Longva T, Eide MS, Skjong R (2010) Determining a required energy efficiency design index level for new ships based on a cost-effectiveness criterion. *Maritime Policy & Management* 37(2):129–143. <https://doi.org/10.1080/03088830903533759>
- Mäkiharju SA, Ceccio SL (2018) On multi-point gas injection to form an air layer for frictional drag reduction. *Ocean Engineering* 147(October 2017):206–214. <https://doi.org/10.1016/j.oceaneng.2017.10.041>, URL <http://linkinghub.elsevier.com/retrieve/pii/S0029801817306492>
- Menter FR (1994) Two-equation eddy-viscosity turbulence models for engineering applications. *AIAA Journal* 32(8):1598–1605. <https://doi.org/10.2514/3.12149>

- Min T, Kim J (2004) Effects of hydrophobic surface on skin-friction drag. *Physics of Fluids* 16(7):L55–L58. <https://doi.org/10.1063/1.1755723>
- Mutton R, Atlar M, Downie M, et al (2005) Drag prevention coatings for marine propellers. In: 2nd International Symposium on Seawater Drag Reduction, Busan, Korea, pp 23–26
- Muzenski S, Flores-Vivian I, Sobolev K (2015) Hydrophobic engineered cementitious composites for highway applications. *Cement and Concrete Composites* 57:68–74. <https://doi.org/10.1016/j.cemconcomp.2014.12.009>, URL <http://dx.doi.org/10.1016/j.cemconcomp.2014.12.009><http://linkinghub.elsevier.com/retrieve/pii/S0958946514002339>
- Nuchturee C, Li T, Xia H (2020) Energy efficiency of integrated electric propulsion for ships - A review. *Renewable and Sustainable Energy Reviews* 134(August):110,145. <https://doi.org/10.1016/j.rser.2020.110145>, URL <https://linkinghub.elsevier.com/retrieve/pii/S1364032120304366>
- Othmer C (2008) A continuous adjoint formulation for the computation of topological and surface sensitivities of ducted flows. *International Journal for Numerical Methods in Fluids* 58(8):861–877. <https://doi.org/10.1002/fld.1770>
- Ou J, Perot B, Rothstein JP (2004) Laminar drag reduction in microchannels using ultrahydrophobic surfaces. *Physics of Fluids* 16(12):4635–4643. <https://doi.org/10.1063/1.1812011>
- Park J, Lim H, Kim W, et al (2011) Design and fabrication of a superhydrophobic glass surface with micro-network of nanopillars. *Journal of Colloid and Interface Science* 360(1):272–279. <https://doi.org/10.1016/j.jcis.2011.04.047>, URL <http://dx.doi.org/10.1016/j.jcis.2011.04.047><http://linkinghub.elsevier.com/retrieve/pii/S0021979711004644>
- Peifer BC, Callahan-Dudley C, Makiharju SA (2020) Air Layer on Superhydrophobic Surface for Frictional Drag Reduction. *Journal of Ship Research* 64(02):118–126. <https://doi.org/10.5957/jsr.2020.64.2.118>, URL <https://onepetro.org/JSR/article/64/02/118/448279/Air-Layer-on-Superhydrophobic-Surface-for>
- Pingen G, Maute K (2010) Optimal design for non-Newtonian flows using a topology optimization approach. *Computers & Mathematics with Applications* 59(7):2340–2350. <https://doi.org/10.1016/j.camwa.2009.08.044>, URL <http://linkinghub.elsevier.com/retrieve/pii/S0898122109006336>
- Romero J, Silva E (2014) A topology optimization approach applied to laminar flow machine rotor design. *Computer Methods in Applied Mechanics and Engineering* 279:268–300. <https://doi.org/10.1016/j.cma.2014.06.029>, URL <http://linkinghub.elsevier.com/retrieve/pii/S0045782514002151>
- Rozvany GIN, Zhou M, Birker T (1992) Generalized shape optimization without homogenization. *Structural Optimization* 4(3-4):250–252. <https://doi.org/10.1007/BF01742754>, URL <http://link.springer.com/10.1007/BF01742754>
- Sánchez-Caja A, Sipilä TP, Pykkänen JV (2009) Simulation of Viscous Flow around a Ducted Propeller with Rudder Using Different RANS-Based Approaches. *First International Symposium on Marine Propulsion* (June):1–8
- Seo J, Mani A (2016) On the scaling of the slip velocity in turbulent flows over superhydrophobic surfaces. *Physics of Fluids* 28(2):025,110. <https://doi.org/10.1063/1.4941769>, URL <http://aip.scitation.org/doi/10.1063/1.4941769>
- Siemens (2018) STAR-CCM+ Documentation - version 13.06
- The International Towing Tank Conference (2021) The Specialist Committee on Energy Saving Methods: Final Report and Recommendations to the 29th ITTC. Tech. rep., URL <https://ittc.info/media/9100/sc-energy-saving-methods.pdf>
- United Nations (2015) Transforming Our World: The 2030 Agenda for Sustainable Development. URL https://www.un.org/ga/search/view_doc

[asp?symbol=A/RES/70/1&Lang=E](#)

- Versteeg HK, Malalasekera W (2007) An introduction to computational fluid dynamics: the finite volume method. Pearson education
- Voronov RS, Papavassiliou DV, Lee LL (2006) Boundary slip and wetting properties of interfaces: Correlation of the contact angle with the slip length. The Journal of Chemical Physics 124(20):204,701. <https://doi.org/10.1063/1.2194019>
- Voronov RS, Papavassiliou DV, Lee LL (2007) Slip length and contact angle over hydrophobic surfaces. Chemical Physics Letters 441(4-6):273–276. <https://doi.org/10.1016/j.cplett.2007.05.013>, URL <http://linkinghub.elsevier.com/retrieve/pii/S0009261407005866>
- Voronov RS, Papavassiliou DV, Lee LL (2008) Review of Fluid Slip over Superhydrophobic Surfaces and Its Dependence on the Contact Angle. Industrial & Engineering Chemistry Research 47(8):2455–2477. <https://doi.org/10.1021/ie0712941>
- Wächter A, Biegler LT (2006) On the implementation of an interior-point filter line-search algorithm for large-scale nonlinear programming. Mathematical Programming 106(1):25–57. <https://doi.org/10.1007/s10107-004-0559-y>, URL <http://link.springer.com/10.1007/s10107-004-0559-y>
- Wang C, Huang S, Chang X, et al (2010) Applying periodic boundary conditions to predict open water propeller performance. Journal of Marine Science and Application 9(3):262–267. <https://doi.org/10.1007/s11804-010-1005-6>
- Zhao X, Best A, Liu W, et al (2021) Irregular, nanostructured superhydrophobic surfaces: Local wetting and slippage monitored by fluorescence correlation spectroscopy. Physical Review Fluids 6(5):054,004. <https://doi.org/10.1103/PhysRevFluids.6.054004>